WILEY ONLINE LIBRARY
Early View publication on
www.wileyonlinelibrary.com
(issue and page numbers not yet assigned;
citable using Digital Object Identifier – **DOI**)

J. Biophotonics 1–10 (2012) / **DOI** 10.1002/jbio.201200111

Journal of
BIOPHOTONICS

FULL ARTICLE

Imaging of *ex vivo* nonmelanoma skin cancers in the optical and terahertz spectral regions

Cecil S. Joseph[**,1], *Rakesh Patel*[2], *Victor A. Neel*[3], *Robert H. Giles*[1], *and Anna N. Yaroslavsky*[*,2,3]

[1] Submillimeter-wave Technology Laboratory, University of Massachusetts Lowell, MA
[2] Advanced Biophotonics Laboratory, University of Massachusetts Lowell, MA
[3] Department of Dermatology, Massachusetts General Hospital, Boston, MA

Received 8 June 2012, revised 11 August 2012, accepted 13 August 2012
Published online 13 September 2012

Key words: optical imaging, terahertz imaging, polarization, nonmelanoma skin cancer

We tested the hypothesis that polarization sensitive optical and terahertz imaging may be combined for accurate nonmelanoma skin cancer (NMSC) delineation. Nine NMSC specimens were imaged. 513 μm and 440 nm wavelengths were used for terahertz and optical imaging, respectively. Histopathology was processed for evaluation. Terahertz reflectance of NMSC was quantified. Our results demonstrate that cross-polarized terahertz images correctly identified location of the tumours, whereas cross-polarized and polarization difference optical images accurately presented morphological features. Cross-polarized terahertz images exhibited lower reflectivity values in cancer as compared to normal tissue. Combination of optical and terahertz imaging shows promise for intraoperative delineation of NMSC.

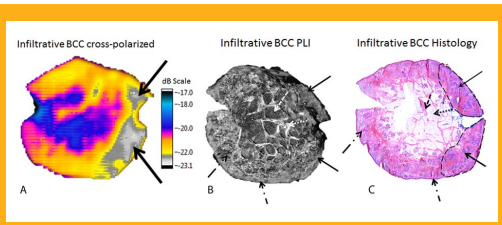

Images of a specimen with infiltrative BCC. (**A**) Cross-polarized Terahertz reflectance image. (**B**) Polarization difference image at 440 nm. (**C**) H & E histopathology. Tumor is outlined (dashed line) in histology and indicated by a solid arrow in Terahertz and optical images. Tumor: solid arrow; collagen: dashed arrow; fat: dotted arrow; epidermis: dash-dot-dash arrow; sebaceous gland: dash-dot-dot-dash arrow.

1. Introduction

With approximately 3.5 million cases diagnosed each year, nonmelanoma skin cancer (NMSC) is the most common form of cancer. NMSC results in about 3000 deaths each year and the cost of treatments is estimated to exceed $ 600 million each year [1]. The most effective form of NMSC treatment is Mohs Micrographic Surgery (MMS) which involves removing cancer layer by layer while simultaneously processing excised tissue for frozen H&E histopathology to map out the cancerous regions. MMS has a success rate of 95% and is the only technique that examines entire surgical margin allowing for complete histological assessment during surgery [2–4]. However MMS is time consuming, labour intensive and costly. Thus, an *in vivo* skin cancer imaging technique could provide a viable alternative to the current methods of intraoperative visualization of cancer margins.

Some techniques that are currently under investigation for non-invasive mapping of skin cancers include reflectance confocal microscopy [5], Raman

* Corresponding author: e-mail: Anna_Yaroslavsky@uml.edu, Phone: +01 978 934 1350, Fax: +01-978-934-1350
** The first and second authors contributed equally to this project.

spectroscopy [6, 7], optical coherence tomography [8, 9], fluorescence polarization [10], multiphoton microscopy [11], fluorescence imaging [12], fluorescence lifetime imaging [13], and high frequency ultrasound [14, 15]. Polarization sensitive optical [16, 17] and terahertz [18–21] imaging have also been proposed.

Continuous wave terahertz imaging (CWT) has the potential to differentiate between nonmelanoma cancers and normal skin. The terahertz region of electromagnetic spectrum extends from 30 to 3000 μm (10 to 0.1 THz) and lies between the microwave and infrared regions. Terahertz radiation is non-ionizing and medical applications of this frequency region are being explored [18–20, 22–25]. Studies show that there is a difference in bound and free water content between normal and cancerous tissue [26, 27]. Due to the lack of commercially available continuous wave terahertz sources, most medical research in terahertz imaging thus far has been focused on terahertz pulsed imaging (TPI). TPI has been used to identify basal cell carcinoma (BCC) both *ex vivo* and *in vivo* [19]. Contrast between cancerous and normal tissue in transmission mode has been demonstrated using a continuous wave terahertz system [21]. One of the disadvantages of terahertz imaging for biomedical applications is the inherent lack of resolution, which prevents terahertz radiation from identifying tissue morphology.

Polarized-light imaging [16, 17, 28] is an optical technique that is capable of obtaining superficial images of thick tissue layers. When the light incident on the sample is linearly polarized, subtraction of two images acquired with the co-polarized ($I_{\parallel}$) and cross-polarized ($I_{\perp}$) light can be used to isolate the single-scattered component, which arises mainly from superficial skin layers [17, 29, 30]. The advantages of the polarized light imaging include the ability to image comparatively thin tissue layers (~30–200 μm in the 380–750 nm spectral range) and to retain a large field of view. Optical images can be acquired within milliseconds. Combination of the large field-of-view, rapid image acquisition, and sufficient lateral resolution enables rapid examination of large surfaces, thus facilitating tumour margin delineation. Our previous work has demonstrated that dye-enhanced multi-spectral reflectance imaging enables reliable delineation of cancerous and normal tissue in more than 91% of cases [17, 31]. However, white light polarization imaging [29] and intrinsic contrast polarization imaging [17] fail to provide sufficiently high resolution and cancer contrast, respectively.

Intrinsic optical imaging yields high resolution, but often lacks contrast for reliable detection of cancer. Terahertz imaging detects intrinsic contrast between healthy and cancerous tissue, but lacks resolution necessary to inspect tissue morphology. In this contribution we are investigating the combination of optical and terahertz imaging for accurate and sensitive delineation of nonmelanoma skin cancer.

2. Experimental

2.1 Continuous-wave terahertz imaging

For the experiments, we used a custom designed CO_2 optically pumped far-infrared (FIR) gas laser [32]. The output power of these CO_2 lasers is in the range of 100–150 W. Tuning the output frequency of the CO_2 laser allows the pumping of different transitions of the gas in the FIR cell. Selecting the gas in the FIR cell and the tuning of the CO_2 laser to the appropriate pump frequency provides the ability to lase different frequencies in the terahertz region. We used the 584 GHz (513 μm) vertically polarized transition in HCOOH, pumped by the 9R28 transition of the CO_2 laser. The measured output power was 10.23 mW. A dielectric (glass) waveguide was placed at the output of the FIR lasers to obtain a Gaussian beam profile [33]. A liquid helium cooled silicon bolometer manufactured by IRLabs was used as a detector. The noise equivalent power (NEP) of the detector was 1.13×10^{-13} W/$\sqrt{\text{Hz}}$ and the responsivity was $2.75 \times 10^{+5}$ V/W. The bolometer had a response time of 5 ms and the gain was 200. A Garnet powdered crystalline quartz window on the bolometer rejected wavelengths below 100 μm.

Figure 1 shows a schematic of the experimental layout. The laser beam was collimated using a TPX lens, passed through a wire grid polarizer to clean up the polarization of the transmitted beam, and focused onto the imaging plane using a short focal length off axis parabolic mirror. The full width at half max (FWHM) was measured to be 0.67 mm at the sample plane. The signal remitted from the sample goes back through the system and, after the focusing mirror, is redirected into the detector arm by a 50–50 Mylar beam splitter. The signal is then

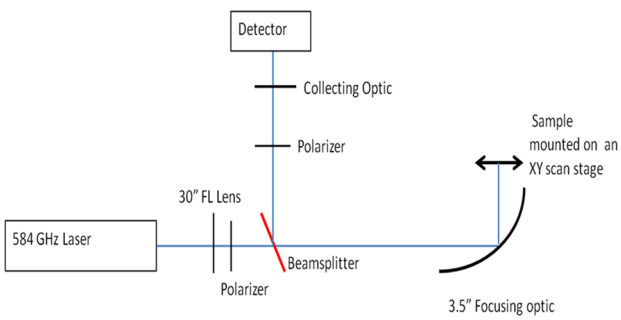

Figure 1 (online color at: www.biophotonics-journal.org) Schematic of terahertz experimental setup.

passed through an analysing wire grid polarizer, which can be oriented to transmit either co-polarized or cross-polarized light and collected using an off axis parabolic mirror and focused into a bolometer. An automated two-axis stage was used to raster scan the sample in the imaging plane. The scanning resolution of both the horizontal and vertical axes was set to 0.1 mm. The laser beam was optically modulated. The modulating frequency served as the reference for a lock-in amplifier. Data acquisition times for the images collected were determined by the speeds of the translation axes used for this experiment and the size of the samples. The dwell time per point in the image was around 150 ms and the system signal-to-noise ratio (SNR) using a lock-in amplifier was 65 dB.

Terahertz images were processed using a Labview^{TM} program that synchronized the sample position in the imaging plane with the return signal from the lock-in amplifier. Co-polarized and cross-polarized images were acquired by selecting the appropriate orientation with the analysing polarizer in the reflectance arm of the system. They were then calibrated against the full-scale return from a flat front surface gold mirror to determine the reflectance. The off sample areas were removed in post-processing and the image was plotted in logarithmic space. The reflected terahertz signal measured from each specimen was quantified pixel by pixel using the formula (1):

$$R_{\mathrm{THz}} = \frac{I_{\mathrm{measured}}}{I_{\mathrm{incident}}} \times 100\,\% \qquad (1)$$

where R_{THz} is the terahertz reflectance value in percentage (%), I_{measured} is the measured reflectance intensity from the sample, and I_{incident} is the measured intensity of the incident beam reflected from a gold front-surface flat mirror.

2.2 Polarized light imaging

Depicted in Figure 2, the bench-top optical imaging system used to acquire reflectance and PLI images of the sample consists of a xenon arc lamp (Lambda LS, Sutter, Novanto, CA) combined with a narrow bandpass filter (full width at half max: 10 nm) to provide monochromatic light at 440 nm [17]. The optical image was detected by a CCD camera (CoolSnap Monochrome Photometrics, Roper Scientific, Tucson, AZ) with an attached 0.5 Rodenstock lens (Linos Photonics, Qioptiq, Luxembourg) resulting in a large field of view (2.8 × 2.5 cm). Linear polarizing filters (Meadowlark Optics, Frederick, CO) were positioned in the beam path incident on and remitted from the sample. These filters allowed collection of

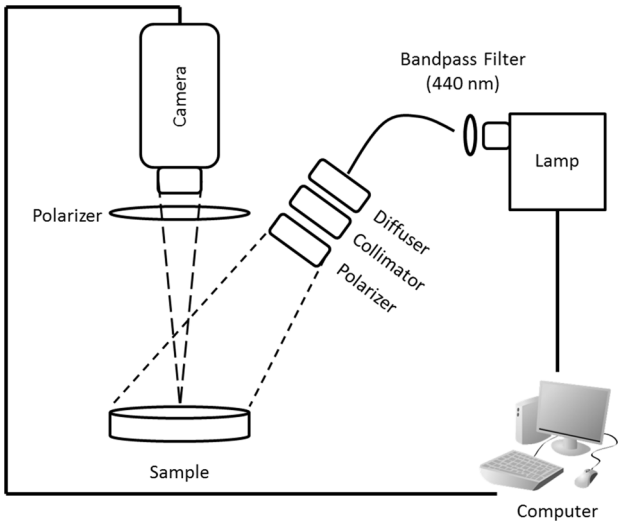

Figure 2 Schematic of polarized light imager.

both co-polarized and cross-polarized reflection images by orienting the analysing polarizer parallel (co-) or perpendicular (cross-) to the polarization of the incident light. Polarization images were processed by applying formula (2), where PLI is the polarized light image, I_{co} is the co-polarized image, I_{cross} is the cross-polarized image, and G is a calibration factor which accounts for any bias in the system towards either polarization.

$$\mathrm{PLI} = I_{\mathrm{co}} - G \times I_{\mathrm{cross}} \qquad (2)$$

The system provided rapid automatic image acquisition (total acquisition time was <100 ms) controlled through Metamorph software (Molecular Devices, Inc., Sunnyvale, CA). The lateral resolution was measured to be better than 15 μm. The calibration factor, G, of the system as described was measured to be 0.98.

2.3 Sample preparation

Fresh thick excess cancer specimens were obtained within 2 hours after Mohs micrographic surgeries performed at the Massachusetts General Hospital under an Institutional Review Board approved protocol. A total of 9 samples from 9 patients (skin types I-III Fitzpatrick scale), including 7 males (median age of 66) and 2 females (median age of 90.5) were collected. Patient demographics are summarized in Table 1, columns 2–4. Their final diagnoses, based on pathologic findings and tumour margin assessments, included 6 basal cell carcinomas and 3 squamous cell carcinomas. The thickness of the specimens varied between 3 and 7 mm. The lateral dimensions were between 10 and 30 mm. All the samples contained stratum corneum, epidermis and

Table 1 Study cases with mean terahertz reflectivity.

Sample Number	Diagnosis	Gender	Age	Normal % reflectance (THz)	Standard Deviation	Cancer % reflectance (THz)	Standard Deviation
1	BCC	Male	76	0.86	±0.13	0.61	±0.071
2	BCC	Female	87	0.92	±0.12	0.80	±0.057
3	BCC	Male	55	0.65	±0.069	0.56	±0.013
4	BCC	Male	88	0.85	±0.11	0.71	±0.023
5	BCC	Male	60	0.84	±0.083	0.73	±0.014
6	BCC	Male	39	0.77	±0.071	0.58	±0.030
7	SCC	Male	75	0.74	±0.12	0.58	±0.018
8	SCC	Female	94	0.86	±0.11	0.77	±0.046
9	SCC	Male	66	1.06	±0.12	0.86	±0.031

dermis. Thicker specimens also contained subcutaneous fat. The specimens were transported to the University of Massachusetts at Lowell on ice in the OCT (Optimal Cutting Temperature) compound within 30 minutes. Then the specimens were thawed and imaged within 6 hours. For imaging, the specimens were covered with a 1 mm thick quartz window. To prevent dehydration during the experiment, the samples were placed on a gauze soaked in pH balanced (pH 7.4) saline solution. To ensure sufficient hydration of the tissue during the experiments, after completing optical imaging, few drops of saline solution were added and the samples were re-mounted for Terahertz imaging.

2.4 Histology processing

En face frozen haematoxylin and eosin (H&E) sections were processed from the imaged specimens in a standard way described in detail elsewhere [2, 34]. These frozen H&E sections were used as a gold standard for evaluation of the results yielded by optical and terahertz images.

2.5 Correlation of terahertz and optical images to histopathology

The correlation of optical and terahertz images to histopathology was performed in a manner similar to that described in [31]. Due to preparation of frozen H&E sections, processed histology sections were slightly distorted in comparison to size and shape of the real samples. This caused discrepancies in correlation of the optical and terahertz sample images to histology. To facilitate a more accurate analysis, we digitized the histological slides and identified four to ten pairs of common features in histology and in the optical images. Then we overlaid optical and histopathological images by applying affine transformations. Normal and cancer areas were subsequently demarcated by a pathologist on the digitized histology image. Corresponding normal and cancer areas were projected from the digitized histology onto the optical and terahertz images.

2.6 Statistical analysis

Reflectance values obtained from terahertz images were averaged for representative normal or cancer areas of each sample. The reflectance values corresponding to cancer and normal respective regions obtained for each sample were averaged over all basal cell carcinomas (BCC), squamous cell carcinomas (SCC), and all the samples (BCC + SCC). To quantify the significance of the differences between normal and cancerous tissue, the data was evaluated using a 1 tailed student's *t*-test for 2 independent populations. The significance test was performed on the mean values averaged over all samples imaged. *P*-values were reported to indicate the significance of the differences.

3. Results and discussion

In total we measured 9 specimens from 9 subjects, which included 6 basal cell carcinomas (BCC) and 3 squamous cell carcinomas (SCC). The final diagnoses were based on the analysis of the frozen H&E histopathology processed during the micrographic surgeries. The information on the imaged specimens is summarized in Table 1 columns 1–4.

A representative sample of basal cell carcinoma is shown in Figure 3. BCC is the most common skin cancer type. It rarely metastasizes. However, because it can cause significant destruction, disfigurement and morbidity by invading surrounding tissues, it is

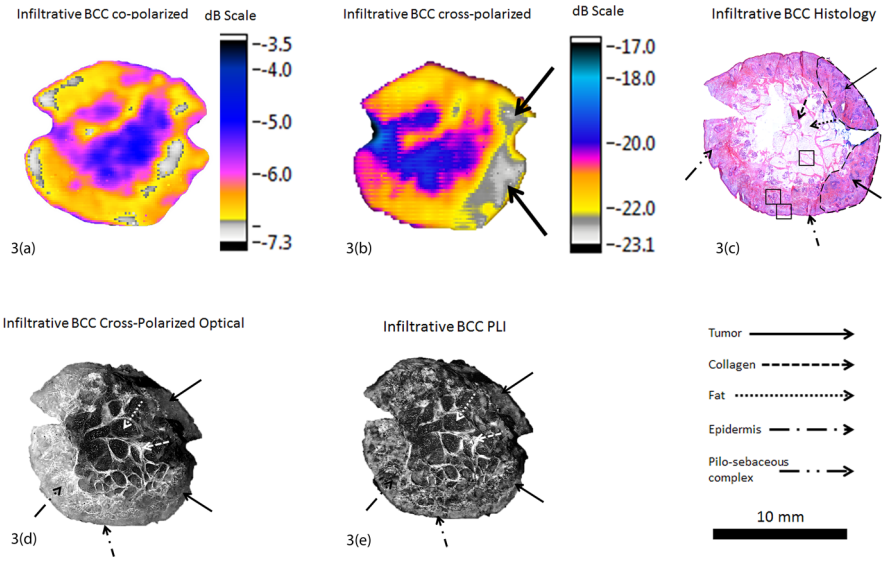

Figure 3 (online color at: www.biophotonics-journal.org) Specimen with infiltrative BCC, (**a**) shows the co-polarized terahertz reflectance image, (**b**) shows the cross-polarized terahertz reflectance image, (**c**) shows the H&E stained histology of a 5 µm frozen section of the tissue, (**d**) shows the cross-polarized optical image, and (**e**) shows the polarized light image.

still considered malignant. In Figure 3a and b, the terahertz co-polarized and cross-polarized images are presented. The tumour is outlined with the black dotted line in the H&E histopathology (Figure 3c). It can be appreciated that the tumour region correlates well with the size and shape of low reflectance areas in the cross-polarized terahertz image (Figure 3b). The location of the tumour is indicated by a solid arrow in the terahertz cross-polarized image (Figure 3b). The co-polarized terahertz image (Figure 3a) does not correlate with the sample histology as well as cross-polarized image. In particular, the areas of lower reflectivity don't correlate with cancer affected area histopathology. The difference in the appearance of the co- and cross-polarized terahertz images is primarily due to specular reflection of the air cover glass and cover glass tissue interfaces, which contribute to the co-polarized image. The majority of Fresnel signal comes from the reflection of the incident radiation on the glass air interface and, therefore, does not contain information on the sample. However, it cannot be rejected from the co-polarized terahertz image due to the geometry of the experiment (Figure 1). In contrast, imaging cross-polarized terahertz signal enables effective removal of the specular reflections, as the Fresnel component is co-polarized with the incident radiation.

The optical reflectance cross-polarized and polarization difference images are presented in Figure 3d and e, respectively. As compared to terahertz images

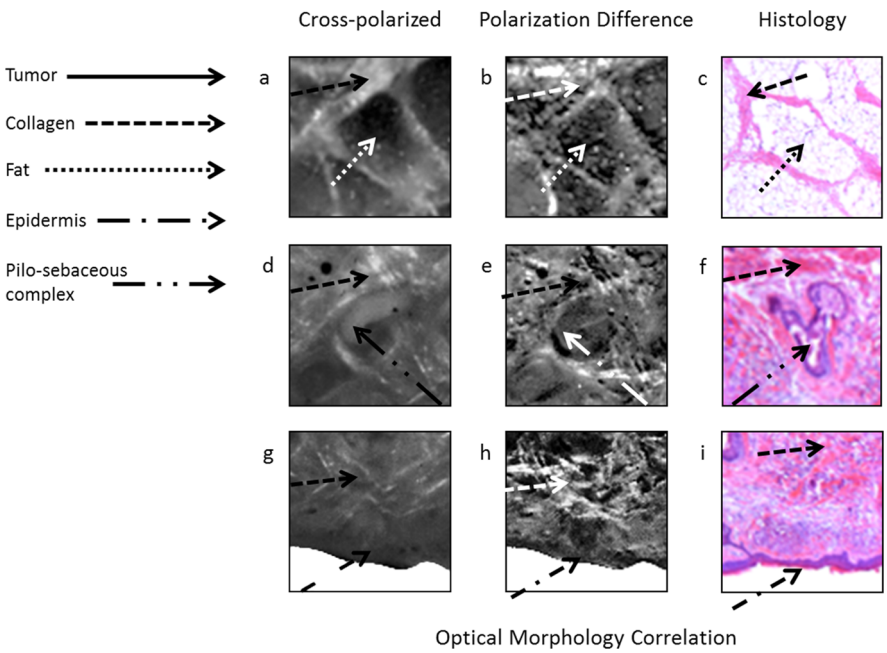

Figure 4 (online color at: www.biophotonics-journal.org) Comparison of magnified high resolution optical and histology images of morphological features, specified from outlined boxes in the sample histology of the infiltrative BCC specimen (Figure 3c).

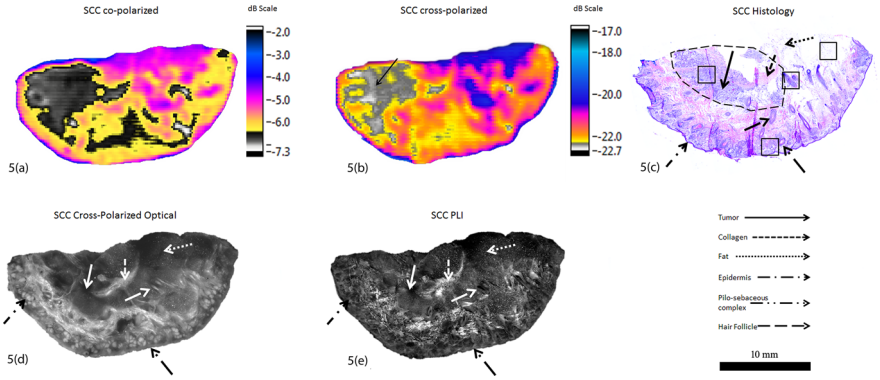

Figure 5 (online color at: www.biophotonics-journal.org) Specimen with SCC, (**a**) shows the co-polarized terahertz reflectance image, (**b**) shows the cross-polarized terahertz reflectance image, (**c**) shows the H & E stained histology of a 5 μm frozen section of the tissue, (**d**) shows the cross-polarized optical image, and (**e**) shows the polarized light image.

(Figure 3a, b), optical images of the same specimen offer higher resolution. The comparison of optical images (Figures 3d, e) to histology (Figure 3c) reveals a close correlation of morphological features as well as overall size and shape of the sample. Polarization difference imaging in skin at 440 nm enables optical sectioning to about 50–70 μm [35]. However, the polarization difference image often provides lower contrast as compared to the cross-polarized image. Therefore, both images were used for tissue morphology analysis. To demonstrate the resolution afforded by optical imaging, the magnified section of regions outlined in histology (Figure 3c: boxes) are presented in Figure 4. The optical images clearly show morphological features such as the epidermis (dash-dot arrow), pilo-sebaceous complex (dash-dot-dot arrow), subcutaneous fat (dot-dot arrow), as well as highly reflective collagen strands (dash-dash arrow). The tumour region (solid arrow), characterized by the loss of skin appendages and collagen appears as a homogenous dark area as seen in Figure 3d, e.

Figure 5 shows a representative specimen with squamous cell carcinoma. While only 20% of non-melanoma cancers are squamous cell carcinomas, they tend to be more aggressive than basal cell cancers. They are more likely to invade fatty tissues beneath the skin and, although this is still uncommon, spread to lymph nodes and/or distant parts of the body. Comparison of the co- and cross-polarized terahertz images (Figure 5a, b) with H&E histopathology presented in Figure 5c, demonstrates that the cross-polarized terahertz image correctly highlights the location of cancer (solid arrow) as in the

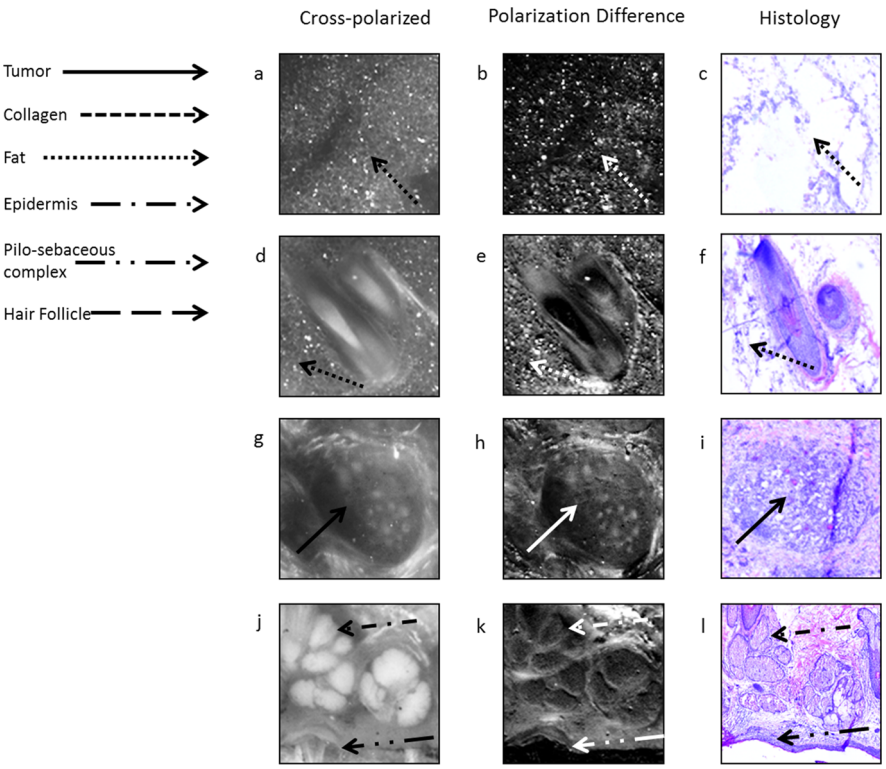

Figure 6 (online color at: www.biophotonics-journal.org) Comparison of magnified high resolution optical and histology images of morphological features, specified from outlined boxes in the sample histology of the SCC specimen (Figure 5c).

case of BCC. Similarly, comparison of the cross-polarized terahertz image (Figure 5b) with the cross-polarized reflectance and the superficial optical images shown in Figure 5d and e, respectively, confirms that the tumour area shows up dark in the optical images, indicating a lack of collagen and loss of structure. Comparison with histology (Figure 5c: tumour outlined with dashed line) shows that terahertz images (Figure 5a, b) have higher contrast of the tumour whereas optical images (Figure 5d, e) delineate tumour affected areas more accurately. Tumour margins, as well as other skin appendages are clearly visible in the optical images. In Figure 6, higher magnification optical images of adipose tissue (Figures 6a–c), hair follicles (Figure 6d–f), tumour lobule (Figure 6g–i), and sebaceous glands (Figure 6j–l) are compared to respective structures in the H&E histopathology image. An obvious resemblance in the appearance of optical and histological images can be well appreciated. Comparison of the optical and terahertz images, presented in Figures 5a, b and 5d, e, respectively, demonstrates the higher resolution offered by optical imaging.

For the terahertz images, the percentage cross polarized reflectivity of representative cancerous areas was compared with the percentage cross polarized reflectivity of representative normal areas on the same sample. Representative cancer and normal areas are the areas of terahertz images, which correspond to cancer affected and normal parts of the specimen according to the gold standard of histopathology. Table 1 summarizes the results for each specimen and histograms for the averaged data for BCC, SCC, and total samples are presented in Figure 7. The average reflectivity values for BCC showed that cancer had lower reflectivity than normal tissue. Similarly, SCC specimens showed the same trend but the reflectivity values were slightly higher than those for BCC samples. This could be because of the low number of SCC specimens ($n = 3$) imaged so it is difficult to draw general conclusions from this data. Overall the average cross polarized percentage reflectivity of the tumour and normal regions for all 9 samples was found to be $0.69 \pm 0.034\%$ and $0.84 \pm 0.010\%$, respectively. The difference between normal and cancer for representative sections averaged over all samples was significant ($p < 0.001$). These results show that even though some differences in the terahertz reflectivity values are expected across the samples, we can expect to find a common threshold value for cancer and normal skin. Nonetheless, as the specimens come from patients of different ages, genders, and tumour sites further work and larger sample size are needed to establish appropriate threshold values.

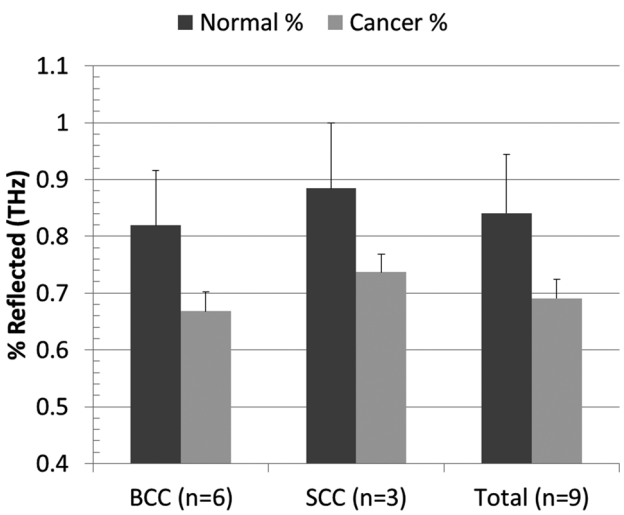

Figure 7 Normal and cancer mean terahertz reflectivity values (%), averaged over all BCC, SCC, and total samples.

In the terahertz images shown in Figure 3a and b, one can easily see that the cross-polarized image correlates better with the sample histology (Figure 3c). This was true for all specimens measured in this study. Although the terahertz images indicate the approximate location of the tumour, they do not accurately demarcate the size and shape of the tumour. On the other hand, optical images provide the morphological detail necessary to outline the extent of the tumour boundaries but lack the level of contrast displayed in terahertz images. As a result, terahertz imaging may be used as a beacon to detect approximate location of tumour nodule and thus guide inspection of the tumour boundaries in optical images. Having accurate tumour boundaries is crucial to ensure full resection of the tumour while preserving as much healthy tissue as possible, especially when the tumour resides on the face.

Another effect that is apparent from our terahertz data is that the cancerous region has a lower reflectivity than the noncancerous region (Figure 7). Our results seemingly contradict the publications reporting higher reflectivity of tumour as compared to normal skin [19, 20]. These reports are substantiated by the fact that cancer has higher refractive index as compared to benign tissue. Therefore, the reflectivity from tumour quartz interface should be higher as compared to that of normal. However, the signal from tissue quartz interface is rejected from cross-polarized images. Thus, their contrast is determined solely by the refractive index fluctuations within the sample volume. There are two possible explanations for lower reflectivity registered from cancer tissue volume as compared to normal. Firstly, due to bound water content, cancer exhibits higher absorption relative to normal skin and therefore leads to lower remitted signal and consequently lower reflectivity of cancerous areas [20]. Secondly, nonmelanoma cancers are defined by their loss of normal skin ar-

chitecture and, given the wavelength of terahertz imaging cancerous skin will look fairly homogenous with minimal refractive index fluctuations within the tumour. In contrast, normal skin has multiple structures (hair follicle, sebaceous gland, adipose tissue, epidermis, etc.) which will cause a greater local refractive index mismatch resulting in higher signal. Interestingly, this observation is similar to what we detect in optical imaging; where tumour affected areas appear darker than normal areas [36].

To the best of our knowledge, we are the first group to use polarization sensitive terahertz imaging for biomedical applications. By implementing cross-polarized reflectance terahertz interrogation we were able to obtain accurate images of skin cancer tissue due to rejecting Fresnel reflections that inevitably contaminate co-polarized component of reflected light. Our results presented in Figure 3 demonstrate that in some cases specular reflections significantly alter the appearance of the co-polarized tissue image (Figure 3a) making delineation of BCC unattainable. In contrast, cross-polarized image of the same tissue (Figure 3b) accurately demarcates cancer as confirmed by histopathology (Figure 3c).

Another possible solution to rejecting the Fresnel component in terahertz imaging would be to illuminate the imaged object at an oblique angle, similar to the optical configuration (Figure 2) presented in this paper. In that case the Fresnel component will not be registered by the detector and both co- and cross-polarized component could be used for accurate imaging. Although realization of the oblique illumination in the terahertz spectral range is challenging, it may be well worth considering since it will almost double the acquired terahertz signal.

4. Conclusion

In summary, we have shown that the combination of polarization sensitive optical and terahertz imaging provides complimentary information and shows promise for intraoperative delineation of nonmelanoma skin cancers. Cross-polarized terahertz imaging correctly detects the location of cancer thus guiding higher resolution optical imaging, which is capable of accessing tissue morphology on a microscopic scale and accurately delineating tumour margins. We have also shown that cross-polarized terahertz reflectivity values are lower for cancerous areas with respect to normal areas. This is an important first step in determining threshold values for accurate detection of nonmelanoma skin cancer using terahertz interrogation. Future studies will focus on designing and building a combined system, developing algorithms for delineating tumour margins, creating fused optical-terahertz images, and optimizing the combined system for clinical use.

Acknowledgements The authors are grateful to Irina Tabatadze for cutting and processing sample histology and Dennis Wirth for digitizing sample histology. The authors would also like to acknowledge Thomas Goyette, Ph.D. Jillian Giles, Chapin Johnson, and Thuquynh Dinh for assisting with data acquisition.

Cecil S. Joseph is a Post-Doctoral Researcher at the Submillimeter-wave Technology Laboratory at the University of Massachusetts Lowell. He received his Ph.D. in Physics from the University of Massachusetts-Lowell in 2010. His research is focused on the development and implementation of terahertz source-receiver technologies for skin cancer delineation, colorectal cancer detection, high resolution terahertz imaging and investigating the response of biological systems to low power terahertz radiation.

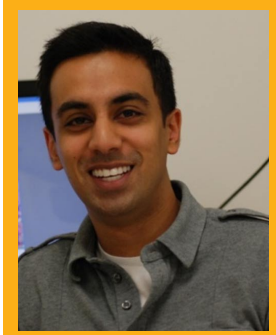

Rakesh Patel is a graduate student pursuing a Ph.D. in medical physics at the Advanced Biophotonics Laboratory at University of Massachusetts, Lowell. He graduated with an MS from University of Southern California and a BS from Boston University both in biomedical engineering. Currently he is involved in researching optical imaging methods (confocal, wide-field, OCT, fluorescence, polarization, etc.) for cancer delineation.

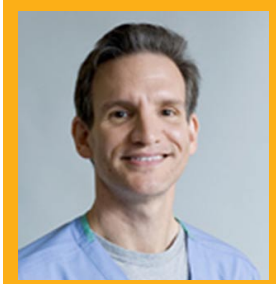

Victor A. Neel has been the head of the dermatologic surgery division in the department of dermatology at Massachusetts General Hospital in Boston since he joined the Harvard Medical School faculty in 2001. Apart from a degree in medicine, he holds a Ph.D. in molecular biology. His research interests include optical imaging in skin and the molecular genetics of skin cancer.

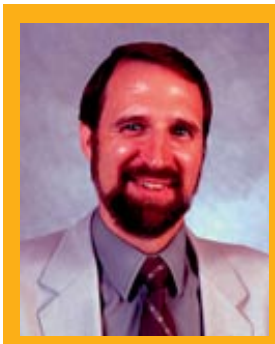

Robert H. Giles Director of UML's Submillimeter-Wave Technology Laboratory and Chairman of the Physics Department, received his Ph.D. at the University of Massachusetts Lowell (UML) in 1986. As a UML researcher since 1982, Dr. Giles has developed, implemented and published a number of advances in terahertz technologies, including the design of polarimetric measurement systems, the development of material characterization methods, the creation of scaled dielectric materials and the fabrication of far-infrared absorbing materials.

Anna N. Yaroslavsky is Associate Professor of Physics and Director of Advanced Biophotonics Laboratory at the University of Massachusetts, USA since 2010. She obtained her Ph.D. in 1999 from the Saratov State University, Saratov, Russia and joined Wellman Center for Photomedicine, Boston, USA in 2000. Since 2005 she has been an Assistant Professor of and since 2010 visiting Associate Professor of Dermatology at Harvard Medical School, USA. Her expertise is in biomedical optics and her work is focused on the development of optical and multimodal technologies for medical applications.

References

[1] H. W. Rogers, M. A. Weinstock, A. R. Harris, M. R. Hinckley, S. R. Feldman, A. B. Fleischer, and B. M. Coldiron, Arch. Dermatol. **146**(3), 283–287 (2010).
[2] F. E. Mohs, Arch. Surg. **42**, 279–295 (1941).
[3] S. J. Salasche and R. A. Amonette, J. Dermatol. Surg. Oncol. **7**(5), 387–394 (1981).
[4] D. J. Wolf and J. A. Zitelli, Arch. Dermatol. **123**, 340–344 (1987).
[5] K. S. Nehal, D. Gareau, and M. Rajadhyaksha, Semin. Cutaneous Med. Surgery **27**(1), 37–43 (2008).
[6] H. Lui, J. Zhao, D. I. McLean, and H. Zeng, Cancer Res. **72**(10), 2491–2500 (2012).
[7] C. A. Lieber, S. K. Majumder, D. Billheimer, D. L. Ellis, and A. Mahadevan-Jansen, J. Biomed. Opt. **13**(2), 024013 (2008).
[8] M. Mogensen, L. Thrane, T. M. Jørgensen, P. E. Andersen, and G. B. E. Jemec, J. Biophoton. **2**, 442–451 (2009).
[9] J. M. Olmedo, K. E. Warschaw, J. M. Schmitt, and D. L. Swanson, J. Amer. Acad. Derm. **55**(3), 408–412 (2006).
[10] Z. Tannous, M. Al-Arashi, S. Shah, and A. N. Yaroslavsky, Lasers Surg. Med. **41**, 10–16 (2009).
[11] J. Paoli, M. Smedh, A. M. Wennberg, and M. B. Ericson, J. Invest. Derm. **128**, 1248–1255 (2008).
[12] B. Stenquist, M. B. Ericson, C. Strandeberg, L. Mölne, A. Rosén, O. Larkö, and A. M. Wennberg, Brit. J. Derm. **154**(2), 305–309 (2006).
[13] N. Galletly, J. McGinty, C. Dunsby, F. Teixeira, J. Requejo-Isidro, I. Munro, D. Elson, M. Neil, A. Chu, P. French, and G. Stamp, Brit. J. Derm. **159**, 152–161 (2008).
[14] C. Harland, S. Kale, P. Jackson, P. Mortimer, and J. Bamber, Brit. J. Derm. **143**, 281–289 (2000).
[15] R. Kleinerman, T. B. Whang, R. L. Bard, and E. S. Marmur, Accepted to J. Amer. Acad. Derm. (2012).
[16] S. L. Jacques, J. R. Roman, and K. Lee, Las.Surg.Med. **26**, 119–129 (2000).
[17] A. N. Yaroslavsky, V. A. Neel, and R. R. Anderson, J. Inv. Derm. **121(2)**, 259–266 (2003).
[18] W. L. Chan, J. Deibel, and D. M. Mittleman, Reports on Progress in Physics. **70**, 1325–1379 (2007).
[19] R. M. Woodward, B. E. Cole, V. P. Wallace, R. J. Pye, D. D. Arnone, E. H. Linfield, and M. Pepper, Phys. Med Biol. **47**, 3853–3863 (2002).
[20] V. P. Wallace, A. J. Fitzgerald, E. Pickwell, R. J. Pye, P. F. Taday, N. Flanagan, and T. Ha, Appl. Spect. **60**(10), 1127–1133 (2006).
[21] C. S. Joseph, A. N. Yaroslavsky, V. A. Neel, T. M. Goyette, and R. H. Giles, Las. Surg. Med. **43**(6), 457–462 (2010).
[22] N. Karpowicz, H. Zhong, J. Xu, K. Lin, J. Hwang, J. Zhang, and X. C. Zhang, Semiconductor Science and Tech. **20**(7), 293–299 (2005).
[23] G. M. Png, J. W. Choi, B. W. H. Ng, S. P. Mickan, D. Abbott, and X.-C. Zhang, Phys. Med. Biol. **53**(13), 3501–3517 (2008).
[24] H. Hoshina, A. Hayashi, N. Miyoshi, F. Miyamaru, and C. Otani, Appl. Phys. Lett. **94**(12), 123901 (2009).
[25] M. A. Brun, F. Formanek, A. Yasuda, M. Sekine, N. Ando, and Y. Eishii, Phys. Med. Biol. **55**(16), 4615–4623 (2010).
[26] M. Gniadecka, O. F. Nielsen, and H. C. Wulf, J. Molecular Structure. **661**, 405–410 (2003).
[27] K. F. A. Ross and R. E. Gordon, J. Microscopy. **128**, 7–21 (1982).
[28] A. N. Yaroslavsky, V. Neel, and R. R. Anderson, Opt. Lett; **29**(17), 2010–2012 (2004).
[29] W. S. Bickel, J. F. Davidson, D. R. Huffman, and R. Kilkson, Proc. Natl. Acad. Sci. USA. **73**, 486–490 (1976).
[30] V. Backman, M. B. Wallace, L. T. Perelman, J. T. Arendt, R. Gurjar, M. G. Muller, Q. Zhang, G. Zonios, E. Kline, T. McGillican, S. Shapshay, T. Valdez, K. Badizadegan, J. M. Crawford, M. Fitzmaurice, S. Kabani, H. S. Levin, M. Seiler, R. R. Dasari, I. Itzkan, J. Van Dam, and M. S. Feld, Nature. **406**(6791), 35–36 (2000).

[31] A. N. Yaroslavsky, E. V. Salomatina, V. Neel, R. Anderson, and T. Flotte, J. Biomed. Opt. **12**(1), 014005 (2007).
[32] T. M. Goyette, J. C. Dickinson, J. Waldman, and W. E. Nixon, Proc. SPIE **4053**, 615–622 (2000).
[33] A. A. Danylov, J. Waldman, T. M. Goyette, A. J. Gatesman, R. H. Giles, K. J. Linden, W. R. Neal, W. E. Nixon, M. C. Wanke, and J. L. Reno, Applied Optics. **46**(22), 5051–5055 (2007).
[34] K. G. Gross, H. K. Steinman, and R. P. Rapini, Mohs Surgery: Fundamentals and Techniques (Mosby Inc, St. Louis, MO, 1999).
[35] A. N. Bashkatov, E. A. Genina, V. I. Kochubey, and V. Tuchin, J. Phys. D: Appl. Phys. **38**(15), 2543–2555 (2005).
[36] A. N. Yaroslavsky, R. Patel, E. Salomatina, C. Li, C. Lin, M. Al-Arashi, and V. Neel, Optics Letters. **37**(4), 644–646 (2012).

